Wheel/rail noise generation due to nonlinear effects and parametric excitation

Anders Nordborg[a)]
The Marcus Wallenberg Laboratory for Sound and Vibration Research, Kungl Tekniska Högskolan, 100 44 Stockholm, Sweden

(Received 16 June 1998; revised 16 January 2002; accepted 22 January 2002)

Two models are developed, one in the time domain and another in the frequency domain, to explain when a wheel/rail noise generation model requires the inclusion of discrete supports, parametric excitation, and the nonlinear contact spring. Numerical simulations indicate the inclusion of discrete supports to describe low frequency response, and also at higher frequencies, especially where the rail is very smooth or has a corrugation/wavelength corresponding to the pinned-pinned frequency. With a corrugation, it may become essential to include the nonlinear contact spring, as contact loss occurs at high corrugation amplitudes. As nonlinearity causes force generation over a broad frequency range, some contributions excite wheel resonances, resulting in high radiation levels, that require the inclusion of wheel/rail nonlinear effects and parametric excitation for accurate prediction. © *2002 Acoustical Society of America.* [DOI: 10.1121/1.1459463]

PACS numbers: 43.50.Lj, 43.40.Cw, 43.50.Ed, 43.40.At [PJR]

I. INTRODUCTION

The most comprehensive and widely used wheel/rail noise model is that developed by Remington and Thompson.[1–4] It is linear, time invariant, performed in the frequency domain, with a validated standard deviation of up to 5 dB, in third-octave bands. They consider roughness only as an excitation mechanism, while suggesting that prediction errors are due to uncertainties in the real roughness level combined with the actual rail/wheel contact position across the rail surface. The conclusion that such an approximation suffices to adequately describe railway noise generation may be premature, requiring evidence from more advanced descriptions of the generation mechanisms. Alternative excitation mechanisms include nonlinearities and parametric excitation due to changing rail and contact receptance with position. In exciting the whole wheel/rail system, a broad insight into force generation would be most helpful in improving noise abatement!

For continuously supported track, nonlinear wheel/rail contact effects are mostly unimportant, unless the roughness level is very high or the static load is very small.[5] Real tracks, however, are discretely supported. It is strongly believed[6,7] that in modifying the contact force, the discrete supports are responsible for corrugation formation on rail surfaces. Of course, it is the same contact force that excites rails and wheels into vibration and noise radiation. Therefore, a realistic rail model should include discrete supports. Two distinct properties are associated with the discrete supports: the sleeper-passing frequency f_s, and the pinned–pinned frequency f_{pp}. The wheels pass the sleepers with the sleeper-passing frequency $f_s = v/l$, where v is the speed and l the sleeper distances. At the pinned–pinned frequency f_{pp}, the bending wavelength of the rail is precisely two sleepers distant $\lambda_{pp} = 2l$, with nodes at the sleeper positions.

In order to investigate when it is necessary to include discrete supports, parametric excitation, and the nonlinear contact spring, two models are presented: one in the time domain and the other in the frequency domain. With each it is possible to either include or exclude a certain property, e.g., discrete supports. Numerical simulations then suggest when this property must be included in the model to accurately describe force generation.

The time domain model, inspired by Heckl's proposal,[8] and by Ilias's and Ripke's wheel/rail interaction models,[7,9] determines the vertical rail deflection by time integrating Green's function of the rail together with force impulses from the wheel/rail contact. Nonlinear Hertzian contact mechanics can be used, less realistic, however, than a discretized contact region allowing for rough surfaces. The wheel is a rigid mass.

The frequency domain model, a simpler version of that developed in Refs. 10 and 11, yields the response by solving a discretized integral equation. Due to the parametric excitation, there is a coupling between different frequency components; the coupling coefficients are essentially the Fourier coefficients of expansion of the varying receptance along the track, described by the track Green's function.

In fact, both models are equivalent formulations of the same problem, once in the time domain and once in the frequency domain. Green's function yields the solution in both cases.

Numerical simulations show that it is necessary to include discrete supports in rail modeling to describe the response at low frequencies, determined by the sleeper-passing frequency f_s, and around the pinned–pinned frequency f_{pp}, usually around 1 kHz—in particular if the rail is very smooth or has a corrugation with a wavelength corresponding to the pinned–pinned frequency. If the rail has a corrugation it may also be necessary to include the nonlinear contact spring, since loss of contact occurs for great corrugation amplitudes, e.g., if the corrugation amplitude r_0 is greater than 15 μm

a)Electronic mail: anders.nordborg@fkt.kth.se

 0001-4966/2002/111(4)/1772/10/$19.00

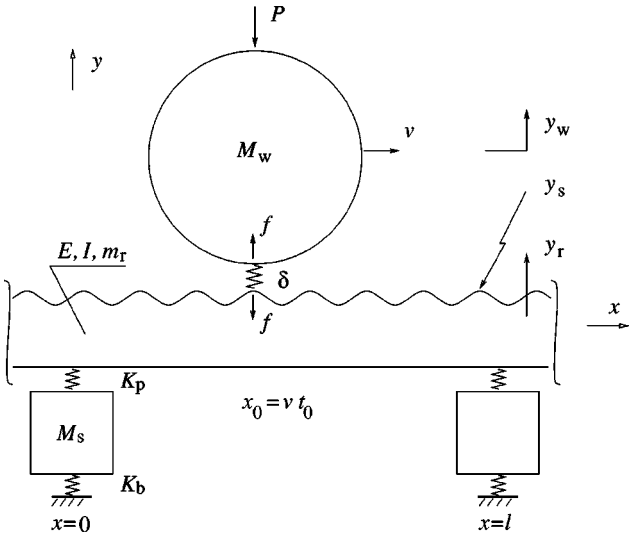

FIG. 1. Time domain wheel/rail interaction model.

when the preload P is 65 kN (for the parameters used in this paper). Nonlinearity causes force generation over a broad frequency range. It may for instance be expected that high frequency contributions will excite wheel resonances, resulting in high noise radiation levels, that require wheel/rail nonlinear effects and parametric excitation for accurate predictions.

II. THEORY

A. Time domain model

A wheel with mass M_w and preload P rolls with forward velocity v over a rail (Fig. 1). The rail has mass m_r per unit length, bending stiffness EI, and a corrugation $y_s = r_0 \sin(2\pi/\lambda_0)x$ on the running surface. The coordinate axis for x points in the forward running direction, and for y upwards in the vertical direction. A perfectly smooth rail implies that $y_s = 0\ \mu$m. The rail is periodically supported at discrete points with spacings l. Each support consists of a spring–mass–spring combination: K_p denotes pad stiffness with loss factor η_p, M_s sleeper mass, and K_b ballast stiffness with loss factor η_b. The compression in the wheel–rail contact region, $\delta_{lin} = y_r + y_s - y_w$, is a function of vertical rail, y_r, and wheel, y_w, deflections plus the deviation from a perfect running surface, y_s. The contact force f, caused by the compression, excites the wheel (upwards) and the rail (downwards). Since this is a time-domain model, rail and wheel deflections, plus the contact force are calculated at each discrete point $x_0 = n\Delta x$, where n is an integer and Δx the space increment, with the corresponding time increment $\Delta t = \Delta x / v$.

1. Rail

The vertical rail deflection, $y_r(x_0, t_0)$, at the moving point, $x_0 = v\,t_0$ (under the wheel), is a convolution of the rail Green's function, $g(x, x_0; t, t_0)$, and the contact force $f(x,t)$,

$$y_r(x_0, t_0) = \int \int g(x, x_0; t, t_0) f(x,t) \mathrm{d}x\, \mathrm{d}t\,.$$

After discretization, and using that the contact force moves forward, $f(x,t) = f(t)\,\delta(x - vt)$,

$$y_r(t_0) = \sum_{k=0}^{K-1} g(x_0 - k\Delta x, x_0; t_0 - k\Delta t, t_0) \times f(t_0 - k\Delta t)\,\Delta t\,, \tag{1}$$

where k is an integer. Note that the force point, $x = x_0 - k\Delta x$, is expressed relative to the response point, x_0. Previous calculations[12] (Appendix B) have provided Green's function in the frequency domain, $G_\omega(x, x_0)$, here first made conjugate symmetric, $G_{-\omega} = G_\omega^*$ (the asterisk denoting complex conjugate), to ensure reality and causality, and then transformed to the time domain by a discrete Fourier transform, $g(x, x_0; t, t_0) = \mathrm{DFT}^{-1}[G_\omega(x, x_0)]$. The force, $f(t_0 - k\Delta t)$, known in the past where $k > 0$, must be found by iterative improvements for the very last time step, $k = 0$. The total number of points, K, must be so great that the impulse from the most distant point, $x_0 - (K-1)\Delta x$, has decayed to a negligible amplitude before it arrives at the response point, x_0.

2. Wheel

The wheel model is the simplest possible: a rigid mass, M_w, acted upon vertically by a constant preload force, P, plus the contact force, f. Numerically, e.g., with Runge–Kutta, solving the ordinary differential equation $M_w \ddot{y}_w(t) = f(t) - P$ (the dots denoting time derivatives) gives the vertical displacement y_w.

3. Contact

This paragraph essentially follows Refs. 7 and 9. The compression of the wheel/rail contact

$$\delta_{lin} = y_r + y_s - y_w, \tag{2}$$

a function of the contact force. Being unknown at the current time step, it can be approximated first with its most recent value, $f(t_0) \leftarrow f(t_0 - \Delta t)$. According to Hertz, the compression distance is a nonlinear function of the contact force f,

$$\delta_H = \left[\frac{2\,f(1-\nu)}{G\sqrt{R_a}} \right]^{2/3} \alpha_\delta\,. \tag{3}$$

Of course, $f \geqslant 0$ always; $f = 0$ implies loss of wheel–rail contact, $\delta_{lin} \leqslant 0$. Here G is the shear modulus, ν Poisson's ratio, and R_a one of the radii of curvature at the contact point. The function α_δ depends on the elliptical shape of the contact area (Fig. 2). Now, solving

$$\delta_{lin} - \delta_H(f) = 0,$$

iteratively, yields the Hertzian contact force f. It is then possible to iterate, with the successive force improvements $f(t_0) \leftarrow f$, until the error $|f(t_0) - f| < \epsilon$, ϵ being a small number. The contact force f plus rail and wheel deflections, y_r and y_w, are now known at the current time step.

B. Frequency domain model

The presentation in this section (also found in Ref. 13), essentially a simpler version of that found in Ref. 10, de-

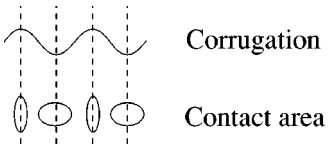

FIG. 2. Contact area variations.

scribes, in three steps, the mathematical framework of the frequency domain model for parametric excitations due to varying contact and track stiffnesses. First, the equation of motion for a mass on a time-varying spring is derived. Second, a continuously supported beam is inserted under the spring. Third, discrete supports are substituted for the continuous foundation under the beam.

1. Mass on a time-varying spring

A rigid mass M moves vertically on a time-varying spring k and a damper c (Fig. 3). Expressing the stiffness in terms of receptance $\alpha(t)=1/k$, the equation of vertical motion $y(t)$ of the mass becomes

$$\alpha(t)\left[M\frac{\mathrm{d}^2y(t)}{\mathrm{d}t^2}+c\frac{\mathrm{d}y(t)}{\mathrm{d}t}\right]+y(t)=b(t),$$

where $b(t)$ is an external base displacement excitation. The time variation of $\alpha(t)$ provides the internal parametric excitation. Fourier expansions of $\alpha(t)$, $b(t)$, and $y(t)$:

$$\alpha(t)=\sum_{n=-\infty}^{\infty}a_n\mathrm{e}^{-\mathrm{i}\Omega_n t},$$

$$b(t)=\sum_{n=-\infty}^{\infty}b_n\mathrm{e}^{-\mathrm{i}\Omega_n t},$$

$$y(t)=\sum_{n=-\infty}^{\infty}y_n\mathrm{e}^{-\mathrm{i}\Omega_n t},$$

yield the system

$$y_m=-\sum_{n=-\infty}^{\infty}a_{m-n}\alpha_{M,c}^{-1}(\Omega_n)y_n+b_m, \tag{4}$$

or $y=Ay+b$ in matrix form, where $-\alpha_{M,c}^{-1}(\Omega_n)=M\Omega_n^2+\mathrm{i}c\Omega_n$. Equation (4) defines the mathematical framework of the frequency domain model for parametric excitations.

2. Wheel on a time-varying contact spring and a continuously supported, corrugated rail

A wheel with vertical receptance $\alpha_{\mathrm{veh}}(\omega)=-1/M_{\mathrm{w}}\omega^2$ and static preload P (including the wheel mass) traverses, with speed v, a corrugated, continuously supported rail (Fig. 15). The track input receptance as "seen" from the wheel consists of Hertzian contact spring receptance $\alpha_{\mathrm{H}}(t)$ and rail receptance $\alpha_{\mathrm{r}}(\omega)$ (Appendix A) in series,

$$\alpha_{\mathrm{H,r}}(t,\omega)=\alpha_{\mathrm{H}}(t)+\alpha_{\mathrm{r}}(\omega)=\sum_{n=-\infty}^{\infty}a_n(\omega)\mathrm{e}^{-\mathrm{i}\Omega_n t}.$$

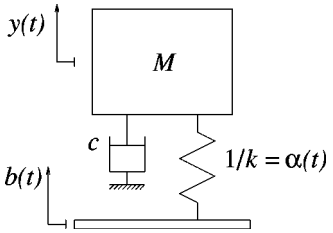

FIG. 3. Mass on a time-varying spring.

(*NB*: Variables t and Ω_n are a transform pair, while ω is a constant.) The coefficients $a_n(\omega)$ go into matrix A of system (4), or

$$y_m=-\sum_{n=-\infty}^{\infty}a_{m-n}(\Omega_n)\alpha_{\mathrm{veh}}^{-1}(\Omega_n)y_n+b_m. \tag{5}$$

To solve system (5) the coefficients of the external excitation vector, b_m, and of the track receptance, $a_{m-n}(\Omega_n)$, must be known. Define the vertical surface deviation due to the corrugation as having the (idealized) form

$$b_{\mathrm{corr}}(t)=-2r_0'\cos\Omega_\nu t$$
$$=-r_0'\mathrm{e}^{-\mathrm{i}\Omega_\nu t}-r_0'\mathrm{e}^{\mathrm{i}\Omega_\nu t}.$$

The corrugation amplitude $2r_0'$ equals r_0 from the time domain model (Sec. II A), $2r_0'=r_0$. The excitation circular frequency $\Omega_\nu=2\pi v/\lambda_0$, ν the index for this frequency, and λ_0 is the corrugation wavelength. That is, there is a trough at $t=0$ $(x=0)$. Due to contact area variations (Fig. 2), the contact receptance has minima in the troughs and maxima on the peaks:

$$\alpha_{\mathrm{H}}(t)=\overline{\alpha}_{\mathrm{H}}-2\tilde{\alpha}_{\mathrm{H}}\cos\Omega_\nu t$$
$$=-\tilde{\alpha}_{\mathrm{H}}\mathrm{e}^{-\mathrm{i}\Omega_\nu t}+\overline{\alpha}_{\mathrm{H}}-\tilde{\alpha}_{\mathrm{H}}\mathrm{e}^{\mathrm{i}\Omega_\nu t}, \tag{6}$$

where $\overline{\alpha}_{\mathrm{H}}$ is the average contact receptance, $\tilde{\alpha}_{\mathrm{H}}$ its (also ideal) variation. The external excitation is a combination of the corrugation and the deflection variation under the static load P,

$$b=b_{\mathrm{corr}}+b_{\mathrm{stat}}, \tag{7}$$

with nonzero components for $m=\pm\nu$, where $b_{\mathrm{corr},\pm\nu}=-r_0'$ and $b_{\mathrm{stat},\pm\nu}=-Pa_\nu$, $a_\nu=-\tilde{\alpha}_{\mathrm{H}}$. It follows from Eq. (5) that the diagonal of the matrix $A_{\mathrm{diag}}=A_{m,m}=-a_0(\Omega_m)\alpha_{\mathrm{veh}}^{-1}(\Omega_m)$ [where $a_0(\Omega_m)=\overline{\alpha}_{\mathrm{H}}+\alpha_{\mathrm{r}}(\Omega_m)$], i.e., the ratio between the average track receptance as "seen" by the wheel, and the wheel receptance. Neglecting internal parametric excitation, but including external roughness excitation changes Eq. (5), short form $y=Ay+b$, to the simpler rolling noise generation presumption

$$y=A_{\mathrm{diag}}y+b_{\mathrm{corr}}, \tag{8}$$

which for a certain circular frequency Ω_ν takes the well-known form

$$y(\Omega_\nu)=\frac{b_{\mathrm{corr}}(\Omega_\nu)}{1+a_0(\Omega_\nu)/\alpha_{\mathrm{veh}}(\Omega_\nu)},$$

the same as that used in most railway noise generation frequency models (e.g., Refs. 1–4).

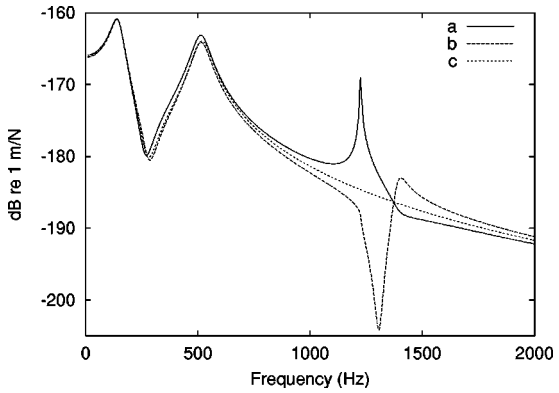

FIG. 4. Vertical rail receptance magnitude: (a) periodic supports, excitation between two sleeper positions: (b) periodic supports, excitation above a sleeper postion; (c) continuous supports. Pinned-pinned resonance at 1224 Hz; pinned-pinned antiresonance at 1305 Hz.

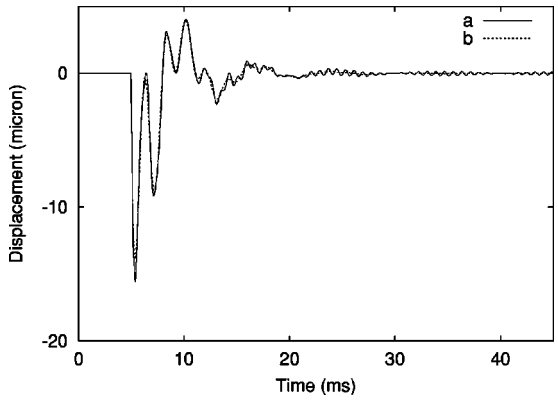

FIG. 5. Moving Green's function , v=60 m/s impluse force, $f(t)=5-65\,\delta(t-t_0)$ kN, t_0=5 ms (sleeper positions at 0,10,20,..., ms). Two rail models: (a) periodic supports; (b) continuous supports.

3. Wheel on a time-varying contact spring and a periodically supported, corrugated rail

Now, the wheel traverses a corrugated, periodically supported, rail (Fig. 17), with the varying point receptance $\alpha_{\mathrm{p}}(x,\omega)$ (Appendix B). The rail surface has the same corrugation and contact receptance variation as before, expressed as a function of the space variable $x=vt$, $\alpha_{\mathrm{H}}(x)=\overline{\alpha}_{\mathrm{H}}-2\tilde{\alpha}_{\mathrm{H}}\cos k_\nu x$, where $k_\nu=2\pi/\lambda_0=\Omega_\nu/v$. The total track input receptance as "seen" by the wheel, $\alpha_{\mathrm{H,p}}(x,\omega)=\alpha_{\mathrm{H}}(x)+\alpha_{\mathrm{p}}(x,\omega)$, with the Fourier coefficients

$$a_n(\omega)=\frac{1}{l}\int_0^l \alpha_{\mathrm{H,p}}(x,\omega)\mathrm{e}^{\mathrm{i}k_n x}\,\mathrm{d}x \tag{9}$$

(where l is the sleeper distances, $k_n=2\pi n/l=\Omega_n/v$) to be inserted into matrix A of system (5), $y=Ay+b$. Since $\alpha_{\mathrm{H,p}}(x,\omega)$ is an even function of x, $a_{-n}(\omega)=a_n(\omega)$. The solution of Eq. (5) with these track Fourier coefficients yields the deflection amplitudes of the wheel, when traversing the corrugated, sleeper-supported rail.

TABLE I. Rail parameters.

Parameter	Value	Description
v	60 m/s	Wheel velocity
M_{w}	600 kg	Wheel mass
P	65 kN	Wheel preload (including wheel mass)
R_{w}	0.46 m	Wheel radius
R_{r}	0.3 m	Rail head radius
E	2.1×10^{11} N/m^2	Rail modulus of elasticity
η_{r}	0.004	Rail loss factor
I	22.5×10^{-6} m^4	Rail moment of area inertia
m_{r}	60 kg/m	Rail mass per unit length
M_{s}	150 kg	(Half) sleeper mass
l	0.6 m	Sleeper spacing
K_{p}	300×10^6 N/m	Pad stiffness
η_{p}	0.15	Pad loss factor
T	0 Nm/rad	Torsional support stiffness
K_{b}	150×10^6 N/m	Ballast stiffness (under a half sleeper)
η_{b}	0.4	Ballast loss factor

III. NUMERICAL RESULTS AND DISCUSSION

A. Rail receptance

The calculations assume parameters according to Table I, unless otherwise stated. Euler beam theory is used, with a reduction of the moment of inertia for a UIC 60 rail to 75% of its tabulated value (30.0×10^{-6} m^4), thus extending the useful frequency region for vertical rail vibrations up to and above 2 kHz.[12,14]

Figure 4 shows vertical rail point receptance calculated with two different models: a periodically supported (Fig. 17) and a continuously supported (Fig. 15) track model. For the periodically supported track, the receptance for two different excitation positions are calculated: between two support positions and above a support position. As a result of having reduced the moment of inertia to 75% of its tabulated value, the pinned–pinned resonance occurs a little above 1200 Hz, which is lower than the 1400 Hz obtained with 100% of the tabulated value. The pinned–pinned antiresonance occurs at about 1300 Hz.

Hitting the rail with an impulse force, following the vertical displacement at a position, moving with velocity v in the x direction, produces the moving Green's function [Eq. (1)]. Figure 5 shows the moving ($v=60$ m/s) Green's functions for periodically and continuously supported rails. For the periodic rail, the impact excitation occurs precisely between two support positions. The model with periodic sup-

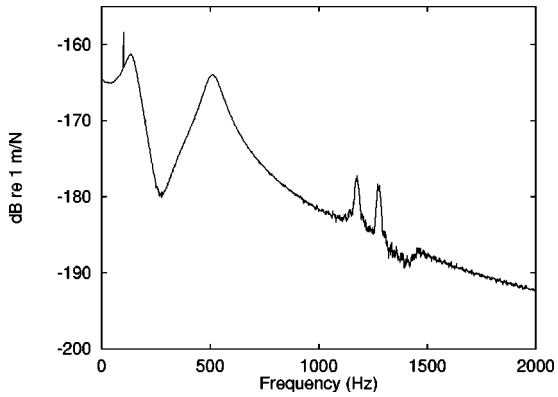

FIG. 6. Moving rail receptance. Velocity $v=60$ m/s. Static force, 65 kN. Random force, 65 kN.

TABLE II. Wheel and contact model parameters.

Parameter	Value	Description
v	60 m/s	Wheel velocity
M_w	600 kg	Wheel mass
P	65 kN	Wheel preload (including wheel mass)
R_w	0.46 m	Wheel radius
R_r	0.3 m	Rail head radius
r_0	25 μm	Corrugation amplitude
λ_0	4.60 cm	Corrugation wavelength

ports has a response at the pinned–pinned frequency, clearly seen as a high frequency component after about 15 ms; otherwise the moving Green's function from the two models are almost identical.

Figure 6 shows the vertical rail point receptance for periodically supported rail, when a static plus a random moving force excite the rail, obtained using the time-domain moving Green's function [Fig. 5 and Eq. (1)]. Forward velocity causes the receptance peak at the pinned–pinned frequency, $f_{pp}=1244$ Hz, to split. The new peaks are approximately located at $f_{pp}(1\pm M)$, where the Mach number $M=v/c_B$, c_B is the bending wave velocity. Since, by definition, the bending wavelength $\lambda_B=2l$ at f_{pp}, $f_{pp}M=f_s/2$, where $f_s=v/l=100$ Hz for $v=60$ m/s, is the sleeper passing frequency, the shifted peaks appear approximately at $f_{pp}\pm f_s/2$. Apart from splitting the f_{pp} peak, forward velocity together with the static load, also cause a peak at the sleeper-passing frequency f_s. The height of the peak is proportional to the static load. Clearly, the moving rail receptance differs from the stationary one at the sleeper-passing frequency and around the pinned–pinned frequency.

B. Time domain model

The calculations assume parameters according to Table I and II, unless otherwise stated. The first calculation (Figs. 7 and 8) simulates a wheel rolling on a corrugated, continuously supported rail (Fig. 15). The contact model is linear and time invariant, not accounting for parametric excitation. The generated contact force has one frequency component only, at the corrugation passing frequency, $f_0=1300$ Hz.

The next calculation simulates a wheel rolling on a corrugated, sleeper-supported rail (Fig. 1). The contact model now accounts for the nonlinear relation between force and deflection/compression (3), as well as parametric excitation in the contact region due to variations of the shape of the contact ellipse (Fig. 2). The corrugation wavelength $\lambda_0=4.60$ cm corresponds to the antiresonance of the pinned–pinned mode, located at 1300 Hz (Fig. 4), a "worst case," but not an unrealistic situation. The corrugation amplitude $r_0=25$ μm.

Because of the discrete supports, the contact force amplitude varies extensively through the sleeper spans (Fig. 9). In the middle of a span, contact loss occurs, causing the contact force to vanish, allowed by the nonlinear contact model. The distance between rail and wheel (Fig. 10), plus the deviation of the rail surface, equals the compression of the wheel/rail contact (2).

The contact force spectrum (Fig. 11) has three main regions. First, at low frequencies, the discrete sleeper supports cause an excitation at the sleeper-passing frequency $f_s=v/l=100$ Hz, plus at its harmonics. Second, corrugation causes an excitation peak at the corrugation-passing frequency $f_0=v/\lambda_0=1300$ Hz, accompanied by smaller peaks 100 Hz apart due to modulation by the sleeper-passing frequency. Third, contact loss and parametric excitation within the contact region, due to shape variations of the contact ellipse, cause an excitation of twice the corrugation-passing fre-

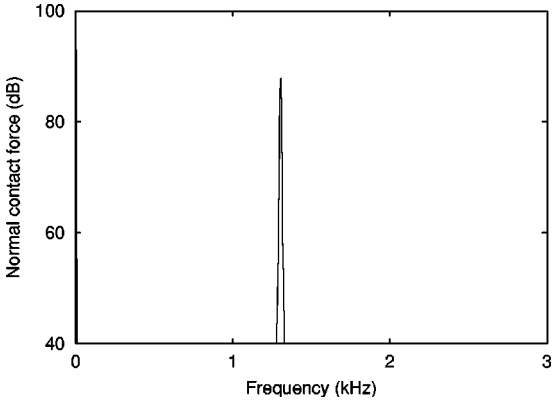

FIG. 8. Normal contact force spectrum for wheel rolling over a corrugated continuously supported rail. Fully linear contact model. Peak at the corrugation-passing frequency $f_0=1300$.

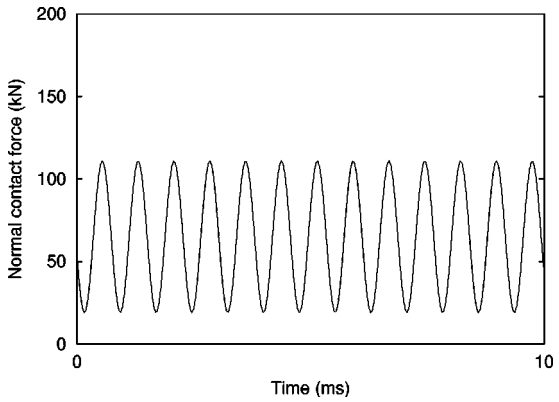

FIG. 7. Normal contact force for wheel rolling over a corrugated, continuously supported rail. Fully linear contact model.

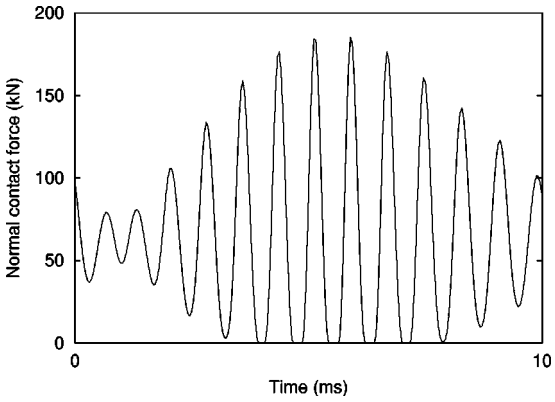

FIG. 9. Normal contact force for wheel rolling one sleeper span over a corrugated rail. Sleeper positions at 0 and 10 ms. Contact model accounting for nonlinearities and parametric excitation.

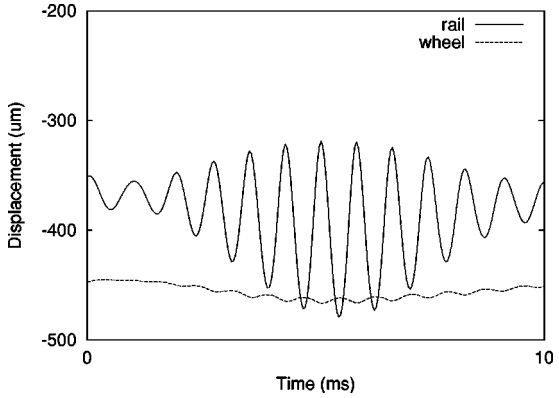

FIG. 10. Rail and wheel deflection for wheel rolling one sleeper span over a corrugated rail. Sleeper positions at 0 and 10 ms. Contact model accounting for nonlinearities and parametric excitation.

quency $2\,f_0 = 2600$ Hz, which is also modulated by sleeper passings.

Comparison of Figs. 11 and 8 clearly enhances the importance of including discrete supports, parametric excitation, and a nonlinear contact spring. The linear, time invariant model (Fig. 8) has a response at one frequency only, while the improved model (Fig. 14) exhibits responses over a broad frequency range. It may for instance be expected that contributions above 2 kHz excite wheel resonances, resulting in high noise radiation levels that require the inclusion of wheel/rail nonlinear effects and parametric excitation for reliable prediction!

C. Frequency domain model

If no wheel/rail contact loss occurs, nonlinearities are small, and the frequency domain model (Sec. II B) accounting for parametric excitation should be appropriate; reducing the corrugation amplitude to 15 μm or increasing the wheel preload to 100 kN guarantees wheel/rail contact (shown by simulations not included here).

The external excitation vector b, Eq. (7), (Fig. 12) represents an equivalent roughness spectrum for a corrugated, sleeper-supported rail. The broadband parts of the spectra correspond to a rough and a smooth rail, respectively. The rough rail has a roughness level of 10 dB per 1/3 octave

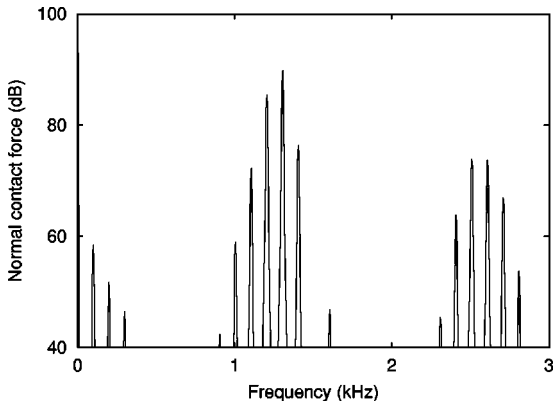

FIG. 11. Normal contact force spectrum for wheel rolling over a corrugated sleeper-supported rail. Contact model accounting for nonlinearities and parametric excitation.

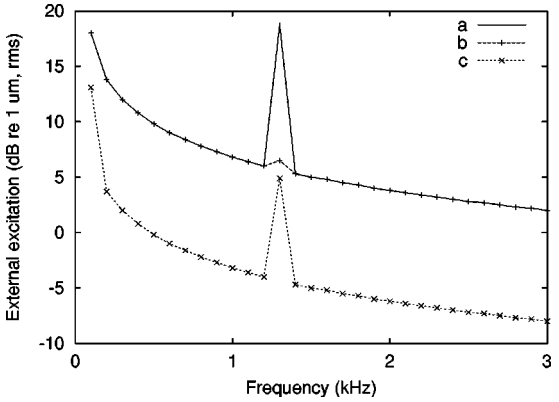

FIG. 12. Equivalent roughness spectrum (external excitation). Three rail surfaces: (a) roughness level $L_{r_0} = 10$ dB, corrugation amplitude $r_0 = 15$ μm, contact receptance variation, 5%; (b) roughness level $L_{r_0} = 10$ dB, corrugation amplitude $r_0 = 3$ μm, contact receptance variation, 0%; (c) roughness level $L_{r_0} = 0$ dB, corrugation amplitude $r_0 = 3$ μm, contact receptance variation, 1%.

bands, and the smooth rail a level of 0 dB per 1/3 octave bands, according to the formula $L_{r_0} = 10\log(r_0^2/r_{\text{ref}}^2)$ (dB), where $r_{\text{ref}} = 1$ μm, rms. Since the frequency resolution here is a constant 100 Hz, the spectra fall off with frequency.

The increased levels at low frequencies are due to varying receptance through the sleeper spans. The peaks at 1.3 kHz are caused by the corrugation with a wavelenth λ_0 of 4.6 cm, and an amplitude r_0 of either 3 or 15 μm. Contact area variations (Fig. 2) cause a contact receptance variation, of 5%, 0%, or 1%.

Figure 13 shows contributions to the response caused by parametric excitation due to discrete sleeper supports and contact receptance variations, i.e., the difference between the levels calculated by Eq. (5), including parametric excitation, and by the approximation (8), excluding parametric excitation. Similarly, as for the time domain model (Fig. 11), there is response at low frequencies due to sleeper passings, and around the pinned–pinned frequency at 1.3 kHz. However, the response around twice the corrugation-passing frequency $2\,f_0 = 2.6$ kHz due to contact area variations is missing here,

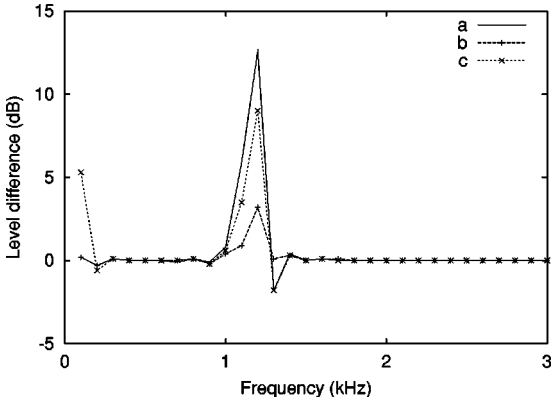

FIG. 13. Parametric excitation contributions: (a) roughness level $L_{r_0} = 10$ dB, corrugation amplitude $r_0 = 15$ μm, contact receptance variation, 5%; (b) roughness level $L_{r_0} = 10$ dB, corrugation amplitude $r_0 = 3$ μm, contact receptance variation, 0%; (c) roughness level $L_{r_0} = 0$ dB, corrugation amplitude $r_0 = 3$ μm, contact receptance variation, 1%.

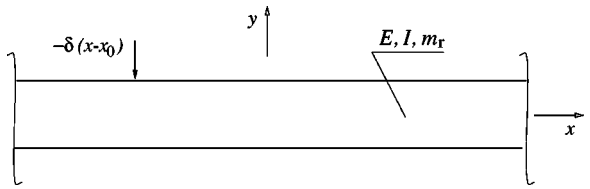

FIG. 14. Infinite beam, excited by a unit point force.

since it is shadowed by the response caused by the broadband part of the roughness spectrum. Obviously, parametric excitation becomes important at low frequencies for smooth rails, and around the pinned–pinned frequency for corrugated rails. Precisely at the corrugation-passing frequency $f_0 = 1.3$ kHz, the response with the model accounting for parametric excitation is a little smaller than that predicted by the pure roughness excitation model, because the deflection variation under the static load P and the surface deviation partly cancel each other out [see Eq. (7)].

IV. CONCLUSIONS

Two models describing wheel/rail noise generation have been developed: one in the time domain and the other in the frequency domain. With each model, it is possible to either include or exclude a certain property, e.g., discrete supports, parametric excitation, and the nonlinear contact spring. Numerical simulations then suggest when this property must be included in the model to accurately describe the force generation.

It is necessary to include discrete supports in rail modeling to describe the response at low frequencies, determined by the sleeper-passing frequency f_s, and around the pinned–pinned frequency f_{pp}, usually around 1 kHz—in particular if the rail is very smooth or has a corrugation with a wavelength corresponding to the pinned–pinned frequency. If the rail has a corrugation it may also be necessary to include the nonlinear contact spring, since loss of contact occurs for great corrugation amplitudes (e.g., if the corrugation amplitude r_0 is greater than 15 μm when the preload P is 65 kN, for the parameters used in this paper). Nonlinearity causes force generation over a broad frequency range. It may for instance be expected that high-frequency contributions excite wheel resonances, resulting in high noise radiation levels, that for accurate prediction require wheel/rail nonlinear effects and parametric excitation to be included.

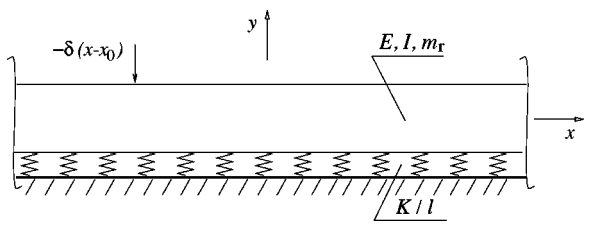

FIG. 15. Continuously supported rail, excited by a unit point force.

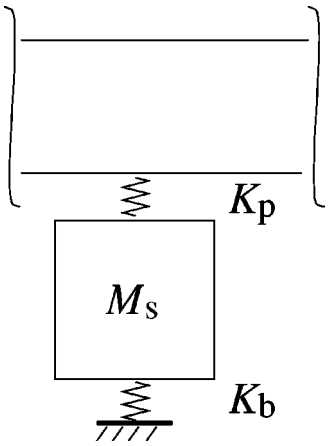

FIG. 16. Rail support: pad stiffness K_p, sleeper mass M_s, and ballast, stiffness K_b.

APPENDIX A: GREEN'S FUNCTION FOR A CONTINUOUSLY SUPPORTED RAIL

A unit point force $\delta(x-x_0)$ excites an infinite beam (Fig. 14), with mass per unit length m_r, and bending stiffness $B=E(1-i\eta_r)I$, where Young's modulus is E, moment of area inertia I, and η_r the loss factor. The equation of motion in the frequency domain is

$$B\left[\frac{d^4}{dx^4}-\frac{m_r\omega^2}{B}\right]G(x|x_0)=\delta(x-x_0), \tag{A1}$$

with the wave number

$$k=\sqrt[4]{\frac{m_r\omega^2}{B}}.$$

A Fourier transform in the x direction, defined by

$$Y(x)=\frac{1}{2\pi}\int_{-\infty}^{\infty}\hat{Y}(\kappa)e^{i\kappa x}d\kappa,$$

$$\hat{Y}(\kappa)=\int_{-\infty}^{\infty}Y(x)e^{-i\kappa x}dx,$$

reduces Eq. (A1) to

$$\hat{G}(\kappa;x_0)(\kappa^4-k^4)=\frac{1}{B}e^{-i\kappa x_0}.$$

An inverse transform,

$$G(x|x_0)=\frac{1}{B}\frac{1}{2\pi}\int_{-\infty}^{\infty}\frac{e^{i\kappa(x-x_0)}}{\kappa^4-k^4}d\kappa,$$

yields Green's function

$$G(x|x_0)=\frac{1}{4Bk^3}(ie^{ik|x-x_0|}-e^{-k|x-x_0|}). \tag{A2}$$

Now, the rail is continuously supported (Fig. 15). Pad stiffness K_p (loss factor η_p), (half) sleeper mass M_s, and ballast stiffness K_b (loss factor η_b)—evenly spread out along the track—comprise the rail foundation. For discrete supports (Fig. 16), the dynamic stiffness at each support point would be

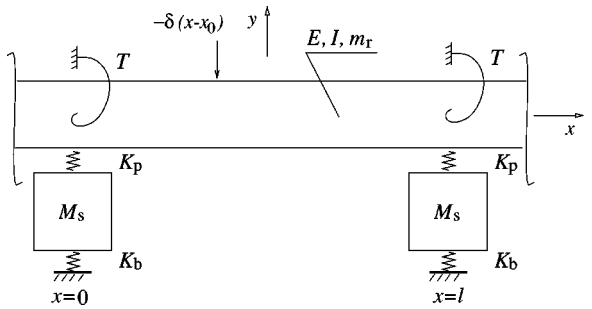

FIG. 17. Discretely supported rail, excited by a unit point force.

$$K=\frac{K_b(1-i\eta_b)-M_s\omega^2}{1+\dfrac{K_b(1-i\eta_b)-M_s\omega^2}{K_p(1-i\eta_p)}}.$$

Here, however, when ''smeared out'' under the rail, the stiffness per unit length is K/l, where l is the nominal sleeper distance for a corresponding sleeper-supported rail. The equation of motion defining Green's function (A1) changes to

$$B\left[\frac{d^4}{dx^4}-\frac{m_r\omega^2}{B}+\frac{K/l}{B}\right]G(x|x_0)=\delta(x-x_0),$$

so the wave number becomes

$$k=\sqrt[4]{\frac{m_r\omega^2-K/l}{B}}.$$

Otherwise, Green's function (A2) remains unchanged. The point input receptance for the continuously supported rail $[\alpha_r(\omega)=G(x_0|x_0)]$,

$$\alpha_r(\omega)=\frac{1}{4Bk^3}(i-1).$$

APPENDIX B: GREEN'S FUNCTION FOR A PERIODICALLY SUPPORTED RAIL

References 11 and 12 in detail derive Green's function for a periodically supported beam, where the support reaction forces are restrained in the vertical. This section (also found in Ref. 15, repeated here for completeness) roughly outlines the derivation adding a rotational degree of freedom to the support reaction (Fig. 17). By including the rotational springs, the solution remains the same, apart from some new terms in the dispersion relation.

1. Support forces

A translational spring at position x by definition reacts with the vertical force $-KY(x)$ on the beam, where $Y(x)$ is the vertical beam displacement at x. The dynamic support stiffness, K, is a complex function, including friction and inertia. Similarly, the complex rotational spring stiffness T reacts on the beam with the moment $M(x)=-TY'(x)$, where the prime denotes a derivative in the x direction, corresponding to the vertical force $M'(x)=-TY''(x)$.

2. Free vibration

The equation of motion, in the frequency domain, for the periodically supported beam is

$$\frac{d^4Y(x)}{dx^4}-k^4Y(x)+\left[\frac{K}{B}Y(x)+\frac{T}{B}\frac{d^2Y(x)}{dx^2}\right]\sum_{n=-\infty}^{\infty}\delta(x-nl)=0, \tag{B1}$$

where

$$k=\sqrt[4]{\frac{m_r\omega^2}{B}}.$$

$B=EI$ is the bending stiffness, m_r the rail mass per length, l the period length, and n an integer. A Fourier transform in the x direction, defined by

$$Y(x)=\frac{1}{2\pi}\int_{-\infty}^{\infty}\hat{Y}(\kappa)e^{i\kappa x}d\kappa,$$

$$\hat{Y}(\kappa)=\int_{-\infty}^{\infty}Y(x)e^{-i\kappa x}dx,$$

reduces Eq. (B1) to

$$\kappa^4\hat{Y}(\kappa)-k^4\hat{Y}(\kappa)+\frac{K}{B}\sum_{n=-\infty}^{\infty}Y(nl)e^{-i\kappa nl}+\frac{T}{B}\sum_{n=-\infty}^{\infty}Y''(nl)e^{-i\kappa nl}=0,$$

where the prime denotes derivative in the x direction. Using Floquet's theorem

$$Y(x+nl)=Y(x)e^{ng}, \tag{B2}$$

it is possible to reach

$$\hat{Y}(\kappa)=\frac{-\dfrac{K}{B}Y(0)\Sigma_{n=-\infty}^{\infty}e^{ng}e^{-i\kappa nl}}{\kappa^4-k^4}+\frac{-\dfrac{T}{B}Y''(0)\Sigma_{n=-\infty}^{\infty}e^{ng}e^{-i\kappa nl}}{\kappa^4-k^4}.$$

After having evaluated the inverse Fourier integrals and infinite sums,[11,12] the solution to this is

$$Y(x,g)=-[KY(0)+TY''(0)]Y_h(x,g), \tag{B3}$$

where the homogeneous solution

$$Y_h(x,g)=\frac{1}{4Bk^3}[\alpha_1(x,g)-\alpha_2(x,g)],$$

with the functions

$$\alpha_1(x,g)=\frac{\sin k(l-x)+e^g\sin kx}{\cos kl-\cosh g},$$

$$\alpha_2(x,g)=\frac{\sinh k(l-x)+e^g\sinh kx}{\cosh kl-\cosh g}.$$

3. Dispersion relation

Putting $x=0$ into Eq. (B3), and its second derivative, yields

$$\begin{pmatrix} 1+KY_{\mathrm{h}}(0,g) & TY_{\mathrm{h}}(0,g) \\ KY''_{\mathrm{h}}(0,g) & 1+TY''_{\mathrm{h}}(0,g) \end{pmatrix} \begin{pmatrix} Y(0) \\ Y''(0) \end{pmatrix} = 0,$$

in matrix form. Evaluation of the determinant yields the dispersion relation,

$$\begin{aligned} \cosh^2 g + \Bigg[& \frac{K}{4Bk^3}(\sinh kl - \sin kl) \\ & + \frac{T}{4Bk}(\sinh kl + \sin kl) - (\cosh kl + \cos kl) \Bigg] \cosh g \\ & + \frac{K}{4Bk^3}(\cosh kl \sin kl - \cos kl \sinh kl) \\ & - \frac{T}{4Bk}(\cosh kl \sin kl + \cos kl \sinh kl) \\ & + \cosh kl \cos kl = 0. \end{aligned}$$

There are four solutions, two for right, and two for left traveling waves, with the propagation coefficients, $g^{\mathrm{r,l}}_{1,2}$, chosen so that all solutions decay away from the excitation point, according to Floquet (B2).

4. Forced vibration

Consider a unit force which excites the beam at $x=x_0$ in the interval $[0,l]$,

$$B\left[\frac{\mathrm{d}^4}{\mathrm{d}x^4} - k^4 + \sum_{n=-\infty}^{\infty} \delta(x-nl)\left(\frac{K}{B} + \frac{T}{B}\frac{\mathrm{d}^2}{\mathrm{d}x^2}\right)\right] G(x|x_0) = \delta(x-x_0),$$

where $G(x|x_0)$ is Green's function. A linear combination of homogeneous solutions, Eq. (B3), which may be rewritten,

$$Y(x,g) = c[\alpha_1(x,g) - \alpha_2(x,g)],$$

where c is a frequency dependent coefficient, constitute Green's function:

$$G(x|x_0) = \begin{cases} c^{\mathrm{r}}_1 Y^{\mathrm{r}}_1(x,g^{\mathrm{r}}_1) + c^{\mathrm{r}}_2 Y^{\mathrm{r}}_2(x,g^{\mathrm{r}}_2) & \text{for } x \geqslant x_0, \\ c^{\mathrm{l}}_1 Y^{\mathrm{l}}_1(x,g^{\mathrm{l}}_1) + c^{\mathrm{l}}_2 Y^{\mathrm{l}}_2(x,g^{\mathrm{l}}_2) & \text{for } x \leqslant x_0. \end{cases} \tag{B4}$$

Matching derivatives at the force point finally determines Green's function. The point input receptance for the periodically supported rail $\alpha_{\mathrm{p}}(x,\omega) = G(x_0|x_0)$.

5. Matching of excitation point boundary conditions

Equation (B4) determines Green's function; matching derivatives at the force point $x=x_0$ leads to

$$\begin{pmatrix} a_{11} & a_{12} & a_{13} & a_{14} \\ a_{21} & a_{22} & a_{23} & a_{24} \\ a_{31} & a_{32} & a_{33} & a_{34} \\ a_{41} & a_{42} & a_{43} & a_{44} \end{pmatrix} \begin{pmatrix} c^{\mathrm{r}}_1 \\ c^{\mathrm{r}}_2 \\ c^{\mathrm{l}}_1 \\ c^{\mathrm{l}}_2 \end{pmatrix} = \frac{1}{Bk^3} \begin{pmatrix} 0 \\ 0 \\ 0 \\ 1 \end{pmatrix}.$$

The matrix coefficients a_{ij} consist of the functions

$$\alpha_1(x,g) = \frac{\sin k(l-x) + \mathrm{e}^g \sin kx}{\cos kl - \cosh g},$$

$$\alpha_2(x,g) = \frac{\sinh k(l-x) + \mathrm{e}^g \sinh kx}{\cosh kl - \cosh g},$$

$$\beta_1(x,g) = \frac{\mathrm{e}^g \cos kx - \cos k(l-x)}{\cos kl - \cosh g},$$

$$\beta_2(x,g) = \frac{\mathrm{e}^g \cosh kx - \cosh k(l-x)}{\cosh kl - \cosh g},$$

evaluated at the excitation point $x=x_0$ as follows:

$$\begin{aligned} a_{11} &= \alpha_1(x_0,g^{\mathrm{r}}_1) - \alpha_2(x_0,g^{\mathrm{r}}_1), \\ a_{31} &= -\alpha_1(x_0,g^{\mathrm{r}}_1) - \alpha_2(x_0,g^{\mathrm{r}}_1), \\ a_{12} &= \alpha_1(x_0,g^{\mathrm{r}}_2) - \alpha_2(x_0,g^{\mathrm{r}}_2), \\ a_{32} &= -\alpha_1(x_0,g^{\mathrm{r}}_2) - \alpha_2(x_0,g^{\mathrm{r}}_2), \\ a_{13} &= -\alpha_1(x_0,g^{\mathrm{l}}_1) + \alpha_2(x_0,g^{\mathrm{l}}_1), \\ a_{33} &= \alpha_1(x_0,g^{\mathrm{l}}_1) + \alpha_2(x_0,g^{\mathrm{l}}_1), \\ a_{14} &= -\alpha_1(x_0,g^{\mathrm{l}}_2) + \alpha_2(x_0,g^{\mathrm{l}}_2), \\ a_{34} &= \alpha_1(x_0,g^{\mathrm{l}}_2) + \alpha_2(x_0,g^{\mathrm{l}}_2), \\ a_{21} &= \beta_1(x_0,g^{\mathrm{r}}_1) - \beta_2(x_0,g^{\mathrm{r}}_1), \\ a_{41} &= -\beta_1(x_0,g^{\mathrm{r}}_1) - \beta_2(x_0,g^{\mathrm{r}}_1), \\ a_{22} &= \beta_1(x_0,g^{\mathrm{r}}_2) - \beta_2(x_0,g^{\mathrm{r}}_2), \\ a_{42} &= -\beta_1(x_0,g^{\mathrm{r}}_2) - \beta_2(x_0,g^{\mathrm{r}}_2), \\ a_{23} &= -\beta_1(x_0,g^{\mathrm{l}}_1) + \beta_2(x_0,g^{\mathrm{l}}_1), \\ a_{43} &= \beta_1(x_0,g^{\mathrm{l}}_1) + \beta_2(x_0,g^{\mathrm{l}}_1), \\ a_{24} &= -\beta_1(x_0,g^{\mathrm{l}}_2) + \beta_2(x_0,g^{\mathrm{l}}_2), \\ a_{44} &= \beta_1(x_0,g^{\mathrm{l}}_2) + \beta_2(x_0,g^{\mathrm{l}}_2). \end{aligned}$$

[1] P. J. Remington, "Wheel/rail rolling noise. I. Theoretical analysis," J. Acoust. Soc. Am. **81**, 1805–1823 (1987).

[2] P. J. Remington, "Wheel/rail rolling noise. II. Validation of the theory," J. Acoust. Soc. Am. **81**, 1824–1832 (1987).

[3] D. J. Thompson, B. Hemsworth, and N. Vincent, "Experimental validation of the TWINS prediction program for rolling noise. 1. Description of the model and method," J. Sound Vib. **193**, 123–135 (1996).

[4] D. J. Thompson, P. Fodiman, and H. Mahé, "Experimental validation of the TWINS prediction program for rolling noise. 2. Results," J. Sound Vib. **193**, 137–147 (1996).

[5] T. X. Wu and D. J. Thompson, "Theoretical investigation of wheel/rail non-linear interaction due to roughness excitation," Veh. Syst. Dyn. **34**, 261–282 (2000).

[6] K. Hempelmann, "Short pitch corrugation on railway rails: A linear model for prediciton," Ph.D. thesis, Technische Universität Berlin, 1994, Fortschritt-Berichte VD1 Reihe 12 Nr. 231.

[7] H. Ilias, "Nichtlineare Wechselwirkungen von Radsatz und Gleis beim Überrollen von Profilstörungen (Nonlinear wheel-rail interaction of a wheelset rolling on a track with profile deviations)," Ph.D. thesis, Technische Universität Berlin, 1996, Fortschritt-Berichte VDI Reihe 12 Nr. 297.

[8] M. Heckl, "Proposal for a railway simulation program," in *A Workshop on*

Rolling Noise Generation (Institute für Technische Akustik, Technische Universität Berlin, October 1989), pp. 128–148.
[9] B. Ripke, ''Hochfrequente Gleismodellierung und Simulation der Fahrzeug-Gleis-Dynamik unter Verwendung einer nichtlinearen Kontaktmechanik (High-frequency track modeling and simulation of vehicle-track dynamics using a nonlinear contact mechanics),'' Ph.D. thesis, Technische Universität Berlin, 1994, Fortschritt-Berichte VDI Reihe 12 Nr. 249.
[10] A. Nordborg, ''Vertical rail vibrations: parametric excitation,'' Acust. Acta Acust. **84**(2), 289–300 (1998).
[11] A. Nordborg, ''Vertical rail vibrations: Noise and structure-borne sound generation,'' Ph.D. thesis, Kungl Tekniska Högskolan, Stockholm, 1995.
[12] A. Nordborg, ''Vertical rail vibrations: Pointforce excitation,'' Acust. Acta Acust. **84**, 280–288 (1998).
[13] A. Nordborg, ''Parametric excitations of a wheel rolling on a corrugated, sleeper-supported track,'' in INTER-NOISE 97-Budapest, Vol. II, pp. 119–122, August 1997.
[14] J.-F. Hamet, ''Railway Noise: Use of the Timoshenko model in rail vibration studies,'' Acust. Acta Acust. **85**, 54–62 (1999).
[15] A. Nordborg, ''Rail/wheel parametric excitation: Laboratory and field measurements,'' Acust. Acta Acust. **85**, 355–365 (1999).